PERGAMON

International Journal of Solids and Structures 39 (2002) 1213–1240

INTERNATIONAL JOURNAL OF SOLIDS and STRUCTURES

www.elsevier.com/locate/ijsolstr

Mesh-free Galerkin simulations of dynamic shear band propagation and failure mode transition

Shaofan Li [a,*], Wing Kam Liu [b], Ares J. Rosakis [c], Ted Belytschko [b], Wei Hao [b]

[a] *Department of Civil and Environmental Engineering, University of California, Berkeley, CA 94720, USA*
[b] *Department of Mechanical Engineering, Northwestern University, 2145 Sheridan Road, Evanston, IL 60208, USA*
[c] *Graduate Aeronautical Laboratories, California Institute of Technology, Pasadena, CA 91125, USA*

Received 9 March 2001; received in revised form 30 July 2001

Abstract

A mesh-free Galerkin simulation of dynamic shear band propagation in an impact-loaded pre-notched plate is carried out in both two and three dimensions. The related experimental work was initially reported by Kalthoff and Winkler (1987), and later re-examined by Zhou et al. (1996a,b), and others.

The main contributions of this numerical simulation are as follows: (1) The ductile-to-brittle failure mode transition is observed in numerical simulations for the first time; (2) the experimentally observed dynamic shear band, whose character changes with an increase of impact velocity, propagating along curved paths is replicated; (3) the simulation is able to capture the details of the adiabatic shear band to a point where the periodic temperature profile inside shear band at μm scale can clearly be seen; (4) an intense, high strain rate region is observed in front of the shear band tip, which, we believe, is caused by wave trapping at the shear band tip; it in turn causes damage and stress collapse inside the shear band and provides a key link for self-sustained instability. © 2002 Elsevier Science Ltd. All rights reserved.

Keywords: Adiabatic shear band; Dynamic shear band propagation; Crack propagation; Failure mode transition; Mesh-free methods; Strain localization; Curved shear band; Multi-physics modeling

1. Introduction

In 1980s, Kalthoff and Winkler published their experimental work on a pre-notched plate subjected to high speed impact (Kalthoff, 1987; Kalthoff and Winkler, 1987). In the experiment (here after referred to as KW problem), a thin metal plate with two pre-notches is impacted by a cylindrical projectile with a flat end. The projectile contacts with the plate in the region between the two notches (see Fig. 1) with speeds from 10 to 100 m/s. The impact initiates a compression wave in the plate, which first creates a predominantly mode II dynamic loading at the notch tips, and then raises temperature around the notch tip regions. The

* Corresponding author. Tel.: +1-510-642-5362; fax: +1-510-643-8928.
E-mail addresses: li@ce.berkeley.edu (S. Li), w-liu@northwestern.edu (W.K. Liu), rosakis@aero.caltech.edu (A.J. Rosakis), t-belytschko@northwestern.edu (T. Belytschko), haowei@nwu.edu (W. Hao).

0020-7683/02/$ - see front matter © 2002 Elsevier Science Ltd. All rights reserved.
PII: S0020-7683(01)00188-3

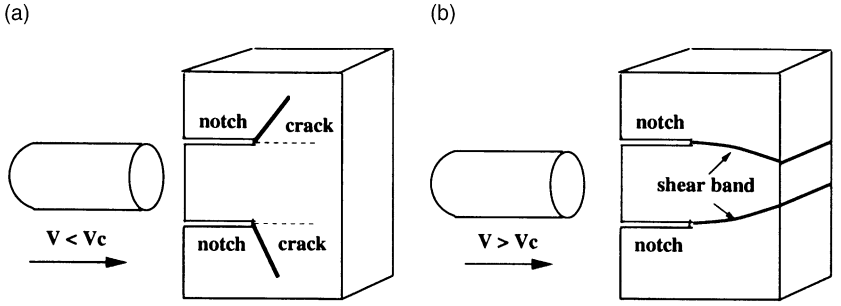

Fig. 1. The KW problem (Kalthoff and Winkler, 1987).

thermo-mechanical behavior of the plate is very complicated and unexpected. The shear dominated loading leads to three different outcomes depending the magnitude of the impact speed: (1) when the impact velocity is low, there is no fracture in the specimen, but massive plastic deformation at notch tip; (2) when the impact velocity exceeds a certain limit, say V_{TF} (subscript "TF" denotes "tensile fracture"), a locally mode I crack initiates from the notch tip and propagates in a direction that forms roughly a 70° angle with the notch line direction (Fig. 1) (in the single notch plate experiment, the cleavage crack path forms 30° angle with the notch line (Zhou et al., 1996b)); (3) when the impact velocity exceeds another (higher) velocity limit, say V_{SB} (subscript "SB" denotes "shear band"), the final failure mode changes: a shear band initiates at the notch tip and propagates through the specimen, which is a purely ductile failure phenomenon.

The significance of the KW problem is that it reveals that under high strain rate shear loading, material failure seems to be dominated by a ductile failure, and the failure mode tends to change from brittle to ductile as the impact velocity increases. The change of failure mode with increase of impact speed is usually referred to as dynamic failure mode transition. The failure mode transition demonstrated in KW experiment contradicts the traditional belief that material failure mode should change from ductile to brittle as the strain rate increases.

After Kalthoff and Winkler's pioneering work, similar experiments have been conducted by several research groups with various materials: mild steel (C300 Maraging steel by Mason et al. (1994); Zhou et al. (1996b), Ti–6Al–4V alloy by Zhou et al. (1996b, 1998), and polymer (polycarbonate) by Ravi-Chandar (1995)). The same failure mode transition has been observed. Zhou et al. (1996a,b, 1998) re-designed the experiment, to refine and improve experimental conditions. In Zhou–Rosakis–Ravichandran experiment (here after referred to as ZRR problem), a single notch plate is used as the target. The main advantage of a single notch specimen is that it eliminates the interference as well as interaction of the diffracted waves between the notches, which occurs in KW's double notch experimental setting, therefore a longer and "cleaner" shear dominated loading can be achieved at the notch tip.

Nonetheless, the main characteristics of the single notch experiment are similar to the double notch experiment, except for an unusual mode switching phenomenon in the intermediate impact velocity range. In the intermediate range impact velocity ($20 < V < 29.6$ m/s), at first a shear band initiates from the notch tip, and is arrested in the middle of the plate; then suddenly a cleavage type crack initiates from the arrested shear band tip. This differs from the behavior observed by Kalthoff that a crack directly initiates from the notch tip. This is a failure mode transition from ductile failure (shear band propagation) to brittle failure (cleavage fracture). [1] At higher impact velocities ($V > 29.6$ m/s), they confirmed Kalthoff's result, i.e. a

[1] Note that two different failure mode transitions are involved in ZRR experiement.

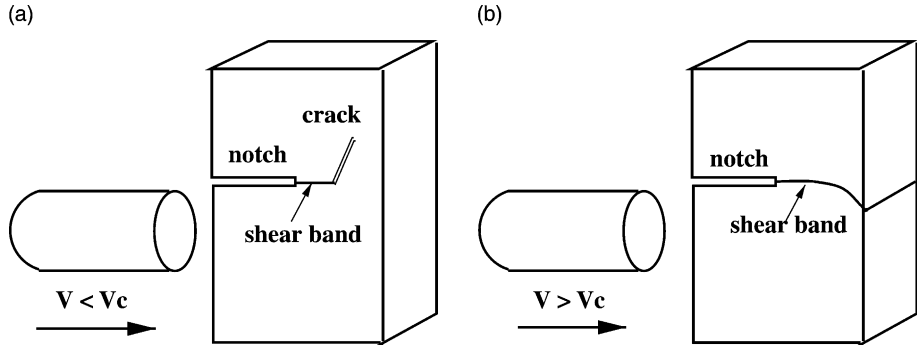

Fig. 2. The ZRR problem.

shear band propagates and penetrates through the specimen without the cleavage fracture. It indicates the dominance of the ductile failure at high strain rate (see Fig. 2).

Reported simulations of the KW and the ZRR experiments have not yet been entirely satisfactory. The challenges are to reproduce the observed shear band propagation speeds and to predict the failure mode transition. The first numerical simulation was reported by Needleman and Tvergaard (1995). To explain the brittle-to-ductile mode transition as impact velocity increases, they noted that high strain rate loading enhances thermal softening, which in turn suppresses the build-up of the maximum hoop stress; thus the system is more prone to ductile failure rather than brittle failure, i.e., the dynamic shear band formation prevails over cleavage crack formation. In their simulation, Zhou et al. (1996a) introduced a viscous fluid-type of constitutive equation for the damage material inside shear band, to mimic its drastic reduction of shear force carrying capability. However, neither computation was able to accurately predict the failure mode transition. In both finite element computations (Needleman and Tvergaard, 1995; Zhou et al., 1996a), the results were mesh dependent. The work reported in Zhou et al. (1996a) is the only successful simulation of the time history of dynamic shear band growth. However, in that work, the shear band was forced to propagate along the finite element edges, a straight line parallel with the pre-notch, in contrast to the curved shear band observed in the real experiment.

Belytschko and Tabbara (1996) used the element-free Galerkin (EFG) method to simulate the KW's double notch experiment by assuming that it is an elasto-dynamic process. Recently, Klein et al. (2000) again used mesh-free methods to simulate the KW problem, with a cohesive micromechanics model—the internal virtual bond constitutive model (Gao and Klein, 1999). In both computations, a crack was found to initiate from the notch tip at about a 70° angle as observed in Kalthoff's experiment. Neither of the above computations was able to replicate the failure mode transition, nor the dynamic shear band propagation. Furthermore, most of the computations conducted so far are two-dimensional (2D).

The present work is aimed at a comprehensive simulation of the ZRR problem (single notch problem). The goal is to investigate the major aspects of the physical deformation and failure processes, which include simulating failure mode transition, dynamic structures of temperatures distribution, stress distribution, inelastic strain/strain rate distributions, and identifying shear band propagation mechanism.

The arrangement of the paper is as follows: Mesh-free methods, in particular the reproducing kernel particle method (RKPM) (Liu et al., 1995a,b, 1997a) is reviewed in Section 2. An explicit mesh-free Galerkin formulation is also outlined in the same section. A thermo-elasto-viscoplastic constitutive model is adopted, which is the adiabatic version of the model used by Zhou et al. (1996a, 1998). By doing so, the rate tangent modulus method of Peirce et al. (1984) is extended to include adiabatic heating. These are discussed in Section 3. Section 4 focuses on the new discoveries of the simulations, such as failure mode transition, temperature reflection, asymptotic strain rate/stress field, and micro-structure of adiabatic shear band.

2. An explicit mesh-free Galerkin formulation

Several mesh-free methods are currently used in computational mechanics. These include the smoothed particle hydrodynamics (Gingold and Monaghan, 1977), the diffuse element method (Nayroles et al., 1992), the EFG method (Belytschko et al., 1994), the RKPM (Liu et al., 1995b, 1996, 1997b), etc. The particular mesh-free method used in this simulation is the RKPM. A detailed account of the method is provided in Liu et al. (1997a) and Li and Liu (1999).

It has been shown recently by Li and Liu (1999, 2000) that mesh-free methods are very efficient in simulations of strain localization problems. The finite element interpolation is generally piece-wise continuous in nature, which inevitably induces mesh alignment sensitivity, a phenomenon in which numerical results depends on local finite element edge orientation, even if the problem is regularized at constitutive level. In contract, the mesh-free interpolation can effectively reduce the mesh alignment sensitivity due to its highly smoothed interpolation scheme, not merely piece-wise continuous but higher order continuity, and its isotropic particle distribution. Another virtue of mesh-free interpolant is its non-local sampling character, which introduces additional numerical "diffusion", or "dissipation" mechanism into simulations. It enhances the numerical algorithm's ability to deal with problems with various discontinuities, though the inherent numerical length scale still depends on the density of particle distribution. In fact, one of the mesh-free methods is called "Diffuse Element Method" (see Nayroles et al., 1992).

Moreover, the class of mesh-free interpolants used in this simulation have extra ability to relieve volumetric locking for displacement based formulation (Belytschko et al., 1994; Chen et al., 1996; Dolbow and Belytschko, 1999), which enables us to implement a straightforward explicit computation. Its advantage in 3D simulation is instrumental.

The basic idea of the RKPM is to construct a proper kernel function on a set of scattered nodal points, such that one can approximate the function of interest through a "reproducing" or "filtering" representation without a mesh,

$$u_\varrho(x) = \mathscr{R}_\varrho u(x) = \int_\Omega \mathscr{K}_\varrho(y-x)u(y)\,\mathrm{d}\Omega \tag{1}$$

where $\mathscr{K}_\varrho(X) := 1/\varrho^n \mathscr{K}(X/\varrho)$, ϱ is the dilation parameter that is associated with the support size of the kernel function, and n is spatial dimension. The RKPM kernel function is compact supported, and usually very smooth, $\mathscr{K}(X) \in C^N(\Omega)$ and $N > 1$. Note that a RKPM representation is a spatial convolution in a strict sense, whereas the finite element interpolation can be viewed as a spatial convolution only in the sense that the kernel function is a generalized function. Assume that in the domain Ω there is a valid particle distribution, $\Lambda := \{1, 2, \ldots, NP\}$. Discretizing Eq. (1) yields a discrete convolution, which is defined as

$$u^h(X) = (\mathscr{K}_\varrho \ *' u)(X) := \sum_{I=\Lambda} \mathscr{K}_\varrho(X_I - X)\Delta V_I u_I \tag{2}$$

where := designates as the symbol of definition. Symbol $*'$ is defined as discrete convolution operator. Eq. (2) represents a non-local interpolation, which is related with discrete convolution. For simplicity, in the rest of the paper, we shall denote $\mathscr{K}_\varrho(X_I - X)\Delta V_I$ as $N_I(X)$. In such "non-local interpolation", any points in the domain, including particle points, are covered by multiple shape functions.

Let $\mathbf{x}$ be the spatial coordinate of a material point and $\mathbf{X}$ be the referential location of that material point. The displacement of the material point is

$$\mathbf{u} := \mathbf{x} - \mathbf{X} \tag{3}$$

The deformation gradient is given by

$$\mathbf{F} := \frac{\partial \mathbf{x}}{\partial \mathbf{X}} \tag{4}$$

A weak form of the balance of linear momentum can be written as (Belytschko et al., 2000)

$$\int_{\Omega_0} \mathbf{P} : \delta\mathbf{F}^T \,\mathrm{d}\Omega_0 = \int_{\Omega_0} \rho_0 \mathbf{B} \cdot \delta\mathbf{u} \,\mathrm{d}\Omega_0 + \int_{\Gamma_0^T} \mathbf{T} \cdot \delta\mathbf{u} \,\mathrm{d}\Gamma_0 - \int_{\Omega_0} \rho_0 \frac{\partial^2 \mathbf{u}}{\partial t^2} \delta\mathbf{u} \,\mathrm{d}\Omega_0 \tag{5}$$

where $\mathbf{T}$ is the prescribed traction on the traction boundary, Γ_0^T, and $\mathbf{P}$ denotes the nominal stress tensor, which can be related to the Kirchhoff stress tensor as $\boldsymbol{\tau} = \mathbf{F} \cdot \mathbf{P}$, and $\mathbf{B}$ is body force per unit mass. For simplicity, the boundary conditions are specified with respect to the referential configuration,

$$\mathbf{n}_0 \cdot \mathbf{P} = \mathbf{T}, \quad \forall\, \mathbf{X} \in \Gamma_0^T; \qquad \mathbf{u} = \bar{\mathbf{u}}, \quad \forall\, \mathbf{X} \in \Gamma_0^u \tag{6}$$

where $\Gamma_0^T \cup \Gamma_0^u = \partial\Omega_0$.

It should be noted that the RKPM interpolant is not able to represent essential boundary conditions via boundary value interpolation. Therefore, an extra term appears in the weak form (5)

$$\int_{\Gamma_0^u} \mathbf{T} \cdot \delta\mathbf{u} \,\mathrm{d}\Gamma_0 \tag{7}$$

because $\delta\mathbf{u} \neq \mathbf{0}$, $\forall\, \mathbf{X} \in \Gamma_0^u$. On how to estimate this term and enforce the essential conditions, the readers may be referred to Li and Liu (2000).

Assume that the trial, and weighting functions have the same form of interpolation,

$$\mathbf{u}^h(\mathbf{X}, t) = \sum_{I=1}^{\mathrm{NP}} N_I(\mathbf{X}) \mathbf{d}_I(t) \tag{8}$$

$$\delta\mathbf{u}^h(\mathbf{X}, t) = \sum_{I=1}^{\mathrm{NP}} N_I(\mathbf{X}) \delta\mathbf{d}_I(t) \tag{9}$$

where NP is the total number of particles.

The weak form (5) will yield the following discrete equations

$$\mathbf{M} \frac{\mathrm{d}^2 \mathbf{u}^h}{\mathrm{d}t^2} = \mathbf{f}^{\mathrm{ext}} - \mathbf{f}^{\mathrm{int}} \tag{10}$$

where $\mathbf{M}$ is the mass matrix, and the external and internal forces are calculated as follows:

$$\mathbf{f}_I^{\mathrm{ext}} = \int_{\Gamma^T} T_i^h(\mathbf{X}, t) N_I \mathbf{e}_i \,\mathrm{d}\Gamma_0 + \int_{\Omega_0} \rho_0 B_i^h(\mathbf{X}, t) N_I(\mathbf{X}) \mathbf{e}_i \,\mathrm{d}\Omega_0 \tag{11}$$

$$\mathbf{f}_I^{\mathrm{int}} = \int_{\Omega_0} P_{Ji}^h \frac{\partial N_I}{\partial X_J} \mathbf{e}_i \,\mathrm{d}\Omega_0 \tag{12}$$

where $\mathbf{e}_i$, $i = 1, 2, 3$ are the unit vectors of the referential coordinate system.

3. Constitutive modeling

It is a well-known fact that the classical rate-independent plasticity theory does not possess an intrinsic length scale, which leads numerical pathologies in simulation of strain localization, such as mesh size and mesh alignment sensitivities.

Several regularization mechanism have been introduced in constitutive modeling. They include: visco-plastic model (Needleman, 1988, 1989); thermal dissipation model (LeMonds and Needleman, 1986a,b; Oliver, 1989; non-local inelastic model (Bazant et al., 1984; Bazant and Pijaudier-Cabot, 1988; Cabot and

Bazant, 1987); strain gradient model or Cosserat type model (Aifantis, 1992; Zbib and Aifantis, 1992; de Borst and Sluys, 1991; de Borst and Pamin, 1996); and others.

In this study, a thermo-viscoplastic constitutive model is adopted. For simplicity, the heat conduction is neglected; thus, the only regularization agent at the constitutive level is viscosity. This approximation may have certain limitations on some aspects of the simulation, such as an accurate determination of evolving shear band width, etc. Nevertheless, the problem is well posed in a mathematical sense, and there is a finite, intrinsic length scale associated with the constitutive parameters (see Needleman, 1988, 1989; Shawki and Clifton, 1989 for details). On the other hand, the mesh-free interpolant introduces diffusion mechanism as well as numerical length scale into the simulation, [2] by the particle distribution density. Mesh size sensitivity is still present in the mesh-free formulation; nevertheless, the mesh alignment sensitivity is significantly suppressed. So far, in most prior simulations of strain localization, the main effort is to simulate the mere appearance of bifurcated deformation modes due to material instability. Nevertheless, how and why such localization zone is able to propagate is still not well understood. A common belief among the researchers is that dynamic shear band propagation is a self-sustained material instability propagation in an auto-catalytic manner.

It should be noted that adiabatic shear band propagation may be viewed as a (weakly) shock wave front *expansion* but different from a (weakly) shock wave front propagation (Hadamard, 1903). Based on this philosophy, dynamic shear band propagation may be simulated by a single constitutive model, and it should happen automatically. Unfortunately, most of prior simulations failed to capture adiabatic shear band propagation.

On the other hand, it is most physicists' belief that shear band is a physical entity, within which significant change in material strength and properties take place. For instance, shear band can be identified a possible phase transformation (see Giovanola, 1988a,b). In this spirit, the constitutive behavior in the localized damage zone in the post-bifurcation phase dictates, or controls, shear band propagation. It is believed that stress collapse inside the strain localization zone in the post-bifurcation phase is crucial for the subsequent propagation of adiabatic shear band, or expansion of strain localization zone, because it allows the dynamic loading continuously be mounted on the shear band tip, and provides driving force for the shear band propagation. This notion has been implicitly suggested by Zhou et al. (1996a), Batra and Nechitailo (1997), and Raftenberg (2000).

The key technical ingredient of simulating dynamic shear band propagation are two: (1) resolving micromechanical length scale that is associated with adiabatic shear band width, and (2) constitutive modeling in post-bifurcation phase, i.e., how to simulate the threshold of stress collapse inside shear band. Note that the threshold of stress collapse is different from the onset strain localization.

3.1. Thermal-viscoplastic model

In inelastic large deformations, the deformation gradient, $\mathbf{F}$, may be decomposed as

$$\mathbf{F} = \mathbf{F}^{e} \cdot \mathbf{F}^{vp} \tag{13}$$

where $\mathbf{F}^{e}$ describes elastic deformations and rigid body rotations, and $\mathbf{F}^{vp}$ represents viscous inelastic deformations. The rate of deformation tensor, $\mathbf{D}$, and the spin tensor, $\mathbf{W}$, are the symmetric and antisymmetric parts of the spatial velocity gradient $\mathbf{L} = \dot{\mathbf{F}} \cdot \mathbf{F}^{-1}$, i.e.

$$\mathbf{D} + \mathbf{W} = \dot{\mathbf{F}} \cdot \mathbf{F}^{-1} = \dot{\mathbf{F}}^{e} \cdot \mathbf{F}^{e^{-1}} + \mathbf{F}^{e} \cdot \dot{\mathbf{F}}^{vp} \cdot \mathbf{F}^{vp^{-1}} \cdot \mathbf{F}^{e^{-1}} \tag{14}$$

[2] In fact, any discretization will bring numerical length scale into numerical simulation, no matter the discretization is mesh based, or mesh free.

and

$$\mathbf{D} := D_{ij}\mathbf{e}_i \otimes \mathbf{e}_j, \quad D_{ij} := \frac{1}{2}\left(\frac{\partial v_i}{\partial x_j} + \frac{\partial v_j}{\partial x_i}\right) \tag{15}$$

$$\mathbf{W} := W_{ij}\mathbf{e}_i \otimes \mathbf{e}_j, \quad W_{ij} := \frac{1}{2}\left(\frac{\partial v_i}{\partial x_j} - \frac{\partial v_j}{\partial x_i}\right) \tag{16}$$

Note that thermal deformation may be considered as eigenstrain, but makes no contribution in geometric decomposition.

We neglect thermo-elastic contribution on internal work, i.e. $\boldsymbol{\tau} : (\mathbf{D}^{\mathrm{e}} + \mathbf{D}^{t}) \approx 0$, where $\mathbf{D}^{t}$ is the rate of deformation due to thermal expansion. Assume that the major part of plastic work is converted into heat (Taylor and Quinney, 1934). The rate form of balance of energy

$$\int_{\Omega} \rho \dot{e}\, \mathrm{d}\Omega + \frac{\mathrm{d}}{\mathrm{d}t}\int_{\Omega} \frac{1}{2}\rho \dot{\mathbf{u}} \cdot \dot{\mathbf{u}}\, \mathrm{d}\Omega = \int_{\partial\Omega} \mathbf{t} \cdot \mathbf{v}\, \mathrm{d}\Gamma - \int_{\partial\Omega} \mathbf{n} \cdot \mathbf{q}\, \mathrm{d}\Gamma \tag{17}$$

may take the form

$$\int_{\Omega_0} \rho_0 C_p \dot{T}\, \mathrm{d}\Omega_0 = \int_{\Omega_0} \chi \boldsymbol{\tau} : \mathbf{D}^{vp}\, \mathrm{d}\Omega_0 + \int_{\Omega_0} \nabla_{\mathbf{X}}(J \cdot \mathbf{F}^{-1} \cdot \boldsymbol{\kappa} \cdot \mathbf{F}^{-T} \cdot \nabla_{\mathbf{X}} T)\, \mathrm{d}\Omega_0 \tag{18}$$

where e is the specific internal energy; $\mathbf{t}$ is the traction; and $\mathbf{q}$ is the heat flux vector through the boundary; C_p is the specific heat at constant pressure used to approximate the specific heat at constant stress.

A local strong form of the energy equation is

$$\rho_0 C_p \frac{\partial T}{\partial t} = \chi \boldsymbol{\tau} : \mathbf{D}^{vp} + \nabla_{\mathbf{X}}\left(J\mathbf{F}^{-1} \cdot \boldsymbol{\kappa} \cdot \mathbf{F}^{-T} \cdot \nabla_{\mathbf{X}} T\right), \quad \forall\ \mathbf{X} \in \Omega_0 \tag{19}$$

Because the whole impact process last a few hundred μs, the effect of heat conduction is negligible over the domain of the specimen. By only considering adiabatic heating, we have

$$\rho_0 C_p \frac{\partial T}{\partial t} = \chi \boldsymbol{\tau} : \mathbf{D}^{vp} \tag{20}$$

By doing so, the coupled thermo-elasto-viscoplastic problem is uncoupled. Thus the momentum equation (5) suffices for constructing Galerkin weak form, and the energy equation (20) is only used in the constitutive update.

A rate form constitutive equation is used

$$\overset{\nabla}{\boldsymbol{\tau}} := \mathbf{C}^{\mathrm{elas}} : (\mathbf{D} - \mathbf{D}^{vp} - \mathbf{D}^{t}) \tag{21}$$

where the Jaumann rate of Kirchhoff stress, $\overset{\nabla}{\boldsymbol{\tau}} := \dot{\boldsymbol{\tau}} - \mathbf{W} \cdot \boldsymbol{\tau} + \boldsymbol{\tau} \cdot \mathbf{W}$. The thermal rate of deformation, $\mathbf{D}^{t}$, is given as

$$\mathbf{D}^{t} = \alpha \dot{T}\mathbf{1} \tag{22}$$

where α is the coefficient of thermal expansion, and $\mathbf{1}$ is the second order unit tensor.

The yield surface of viscoplastic solid is of the von Mises type,

$$f(\bar{\sigma}, \kappa) = \bar{\sigma} - \kappa = 0 \tag{23}$$

$$\bar{\sigma}^2 = \frac{3}{2} s_{ij} s_{ij} \tag{24}$$

$$s_{ij} = \tau'_{ij} - \alpha_{ij} \tag{25}$$

$$\tau'_{ij} = \tau_{ij} - \frac{1}{3} tr(\boldsymbol{\tau}) \delta_{ij} \tag{26}$$

$$\bar{\epsilon} := \int_0^{\mathrm{t}} \sqrt{\frac{2}{3} \mathbf{D}^{vp} : \mathbf{D}^{vp}} \, \mathrm{d}t \tag{27}$$

where α_{ij} is the back stress for kinematic hardening.

A thermo-elasto-viscoplastic material model is adopted (see Zhou et al., 1996a), which is described as

$$D_{ij}^{vp} := \bar{\eta}(\bar{\sigma}, \bar{\epsilon}, T) \frac{\partial f}{\partial \sigma_{ij}} \tag{28}$$

$$\bar{\eta} = \dot{\epsilon}_0 \left[\frac{\bar{\sigma}}{g(\bar{\epsilon}, T)} \right]^m \tag{29}$$

$$g(\bar{\epsilon}, T) = \sigma_0 [1 + \bar{\epsilon}/\epsilon_0]^N \left\{ 1 - \delta \left[\exp\left(\frac{T - T_0}{\kappa} \right) - 1 \right] \right\} \tag{30}$$

where m is the power index, $\dot{\epsilon}_0$ is the referential strain rate, σ_0 is yield stress, $\epsilon_0 = \sigma_0/E$, and δ is the thermal softening parameter.

The constitutive update largely follows the rate tangent modulus method proposed by Peirce et al. (1984), which has been used in the context of thermo-viscoplasticity by LeMonds and Needleman (1986a,b). The essence of the rate tangent modulus method is to approximate a function of time in the interval, $t_{n+\theta} \in [t_n, t_{n+1}]$ $\theta \in [0, 1]$, as

$$f_\theta := (1 - \theta) f_n + \theta f_{n+1} \tag{31}$$

If we choose the predicted velocity field at t_{n+1} as $\mathbf{v}_{n+1}^{\mathrm{trial}} = \mathbf{v}_n + \Delta t \mathbf{a}_n$, it follows that

$$\mathbf{v}_\theta = (1 - \theta)\mathbf{v}_n + \theta \mathbf{v}_{n+1}^{\mathrm{trial}} = \mathbf{v}_n + \theta \Delta t \mathbf{a}_n \tag{32}$$

$$\mathbf{u}_\theta = (1 - \theta)\mathbf{u}_n + \theta \mathbf{u}_{n+1} = \mathbf{u}_n + \Delta t \theta \mathbf{v}_n + \theta^2 \Delta t^2 \mathbf{a}_n \tag{33}$$

$$\mathbf{L}_\theta = \mathbf{v}_\theta \overleftarrow{\nabla}_{\mathbf{x}} = \left(\mathbf{v}_\theta \overleftarrow{\nabla}_{\mathbf{X}} \right) \cdot \mathbf{F}_{n+1}^{-1} \tag{34}$$

$$\mathbf{D}_\theta = \tfrac{1}{2}\left(\mathbf{L}_\theta + \mathbf{L}_\theta^T \right) \tag{35}$$

$$\mathbf{W}_\theta = \tfrac{1}{2}\left(\mathbf{L}_\theta - \mathbf{L}_\theta^T \right) \tag{36}$$

For $\theta = 1/2$, the predicted step, or trial step corresponds to the central difference scheme. By following Eqs. (32)–(36), the kinematical variables can be calculated at the configuration $t_{n+\theta}$.

The main task here is to update the Kirchhoff stress:

$$\boldsymbol{\tau}_{n+1} = \boldsymbol{\tau}_n + \dot{\boldsymbol{\tau}}_\theta \Delta t \tag{37}$$

$$\dot{\boldsymbol{\tau}}_\theta \approx \overset{\nabla}{\boldsymbol{\tau}}_\theta + \mathbf{W}_\theta \cdot \boldsymbol{\tau}_n + \boldsymbol{\tau}_n \cdot \mathbf{W}_\theta^T \tag{38}$$

To accomplish this, we first set

$$\dot{\bar{\epsilon}}_\theta = (1 - \theta)\dot{\bar{\epsilon}}_n + \theta \dot{\bar{\epsilon}}_{n+1} \tag{39}$$

where $\dot{\bar{\epsilon}}_{n+1}$ is approximated by a first order Taylor series expansion in $\bar{\sigma}$, $\bar{\epsilon}$ and T, i.e.

$$\dot{\bar{\epsilon}}_{n+1} = \dot{\bar{\epsilon}}_n + \Delta t\left(\left.\frac{\partial\dot{\bar{\epsilon}}}{\partial\bar{\sigma}}\right|_n \dot{\bar{\sigma}}_\theta + \left.\frac{\partial\dot{\bar{\epsilon}}}{\partial\bar{\epsilon}}\right|_n \dot{\bar{\epsilon}}_\theta + \left.\frac{\partial\dot{\bar{\epsilon}}}{\partial T}\right|_n \dot{T}_\theta\right) \tag{40}$$

Evaluate other state variables at $t_{n+\theta} = (n+\theta)\Delta t$,

$$\mathbf{D}^{vp}_\theta = \dot{\bar{\epsilon}}_\theta \mathbf{p}_n \tag{41}$$

$$\overset{\nabla}{\boldsymbol{\alpha}}_\theta = b\mathbf{D}^{vp}_\theta \tag{42}$$

$$\dot{\boldsymbol{\alpha}}_\theta = \overset{\nabla}{\boldsymbol{\alpha}}_\theta + \mathbf{W}_\theta \cdot \boldsymbol{\alpha}_n + \boldsymbol{\alpha}_n \cdot \mathbf{W}^T_\theta \tag{43}$$

$$\boldsymbol{\alpha}_{n+1} = \boldsymbol{\alpha}_n + \dot{\boldsymbol{\alpha}}_\theta \Delta t \tag{44}$$

where $\mathbf{p} := (3/2)(\mathbf{s}'/\bar{\sigma})$

Since $\mathbf{p}_\theta$ and $\boldsymbol{\alpha}_\theta$ are unknown in the configuration at Ω_n, inconsistent approximations are made $\mathbf{p}_\theta \approx \mathbf{p}_n$, $\boldsymbol{\alpha}_\theta \approx \boldsymbol{\alpha}_n$ in the explicit calculation.

In isotropic hardening

$$\mathbf{D}^{vp} = \frac{3}{2}\frac{\dot{\bar{\epsilon}}}{\bar{\sigma}}\boldsymbol{\tau}' \tag{45}$$

hence

$$\boldsymbol{\tau} : \mathbf{D}^{vp} = \left(\boldsymbol{\tau}' + \frac{1}{3}tr(\boldsymbol{\tau})\mathbf{1}\right) : \left(\frac{3}{2}\frac{\dot{\bar{\epsilon}}}{\bar{\sigma}}\boldsymbol{\tau}'\right) = \frac{3}{2}\frac{\dot{\bar{\epsilon}}}{\bar{\sigma}}\boldsymbol{\tau}' : \boldsymbol{\tau}' = \bar{\sigma}\dot{\bar{\epsilon}} \tag{46}$$

Eq. (20) becomes

$$\frac{\partial T}{\partial t} = \frac{\chi}{\rho_0 C_p}\bar{\sigma}\dot{\bar{\epsilon}} \tag{47}$$

Utilizing Eq. (47), we propose the following *monolithic* or *simultaneous* rate tangent modulus scheme. Substituting Eq. (47) at time $t_{n+\theta} = (n+\theta)\Delta t$ into Eq. (40), we have

$$\dot{\bar{\epsilon}}_{n+1} = \dot{\bar{\epsilon}}_n + \Delta t_n\left\{\left.\frac{\partial\dot{\bar{\epsilon}}}{\partial\bar{\sigma}}\right|_n \dot{\bar{\sigma}}_\theta + \left.\frac{\partial\dot{\bar{\epsilon}}}{\partial\bar{\epsilon}}\right|_n \dot{\bar{\epsilon}}_\theta + \left.\frac{\partial\dot{\bar{\epsilon}}}{\partial T}\right|_n \left(\frac{\chi}{\rho_0 C_p}\bar{\sigma}_\theta\dot{\bar{\epsilon}}_\theta\right)\right\} \tag{48}$$

Substituting Eq. (48) into Eq. (39) and solving for $\dot{\bar{\epsilon}}_\theta$ yield

$$\dot{\bar{\epsilon}}_\theta = \frac{\dot{\bar{\epsilon}}_n}{1+\xi_\theta} + \frac{1}{H_\theta}\frac{\xi_\theta}{1+\xi_\theta}\mathbf{P}_\theta : \mathbf{D}_\theta \tag{49}$$

where

$$\begin{aligned} H_\theta &:= \frac{3E}{2(1+\nu)} - \left.\frac{\partial\dot{\bar{\epsilon}}/\partial\bar{\epsilon}}{\partial\dot{\bar{\epsilon}}/\partial\bar{\sigma}}\right|_n - \left.\frac{\partial\dot{\bar{\epsilon}}/\partial T}{\partial\dot{\bar{\epsilon}}/\partial\bar{\sigma}}\right|_n \frac{\alpha\chi}{\rho_0 C_p}\bar{\sigma}_\theta \\ &\approx \frac{3E}{2(1+\nu)} - \left.\frac{\partial\dot{\bar{\epsilon}}/\partial\bar{\epsilon}}{\partial\dot{\bar{\epsilon}}/\partial\bar{\sigma}}\right|_n - \left.\frac{\partial\dot{\bar{\epsilon}}/\partial T}{\partial\dot{\bar{\epsilon}}/\partial\bar{\sigma}}\right|_n \frac{\alpha\chi}{\rho_0 C_p}\bar{\sigma}_n \end{aligned} \tag{50}$$

$$\mathbf{P}_\theta := \mathbf{C}^{\text{elas}} : \mathbf{p}_\theta \approx \mathbf{C}^{\text{elas}} : \mathbf{p}_n \tag{51}$$

$$\xi_\theta = \theta \Delta t \left(\frac{\partial \dot{\bar{\epsilon}}}{\partial \bar{\sigma}} \right)_n H_\theta \tag{52}$$

Note that since we do not know the stress state in the configuration $\Omega_{n+\theta}$, in an explicit update we approximate σ_θ by σ_n in the calculations of H_θ, $\mathbf{P}_\theta$, as well as of ξ_θ. This assumption may have been implied in the original derivation of Peirce et al. (1984).

Subsequently, the Jaumann rate of the Kirchhoff stress is evaluated as

$$\overset{\nabla}{\boldsymbol{\tau}}_\theta = \mathbf{C}_\theta^{\tan} : \mathbf{D}_\theta - \left\{ \frac{\dot{\bar{\epsilon}}_n}{1+\xi_\theta} \right\} \left[\mathbf{P}_\theta + 3K\alpha \frac{\chi \bar{\sigma}_\theta}{\rho C_p} \mathbf{1} \right] \tag{53}$$

where

$$\mathbf{C}_\theta^{\tan} = \mathbf{C}^{\text{elas}} - \frac{\xi_\theta}{H_\theta(1+\xi_\theta)} \left[\mathbf{P}_\theta \otimes \mathbf{P}_\theta + (3\lambda + 2\mu)\alpha \frac{\chi \bar{\sigma}_n}{\rho_0 C_p} \mathbf{1} \otimes \mathbf{P}_\theta \right] \tag{54}$$

is the adiabatic tangent stiffness, which is not symmetric. Assuming that $\bar{\epsilon}_\theta$ and $\bar{\sigma}_\theta$ are available after the stress update, the temperature can then be updated at each quadrature point as

$$T_{n+1} = T_n + \dot{T}_\theta \Delta t \tag{55}$$

3.2. Constitutive modeling in post-bifurcation phase

After initial thermal softening, material instability occurs, which leads to strain localization. Based on Marchand and Duffy's well-known experiment on dynamic shear band propagation (Marchand and Duffy, 1988), there are three stages in the development of an adiabatic shear band. In stage I, before, or onset of the strain localization, the plastic strain distribution is homogeneous; in stage II, right after initial localization, the plastic strain distribution become inhomogeneous, but the amount and width of the localized deformation remain same; in stage III, there is drastic reduction of flow stress, the nominal strain becomes quite large, from 40% to more than 1000%, and changes rapidly from one location to another, indicating spatial oscillation, or fluctuation of strain rate distribution. The most salient characteristics of stage III strain localization is that the material drastically loses its shear stress carrying capacity. This phenomenon is called *stress collapse*, and has been predicted by Wright and his colleagues in their theoretical analysis (Wright and Batra, 1985; Wright and Walter, 1987). Apparently, there is a critical strain, or threshold for such stress collapse. Molinari and Cliffton (1987) calculated the critical nominal strain at which the stress collapses. Their result is called the Molinari–Clifton condition. In fact, Gioia and Ortiz (1996) showed that when the Molinari–Clifton condition is met, steady adiabatic boundary layers collapse into a vortex sheet. Nevertheless, how to implement the Molinari–Clifton condition in numerical simulations is still an open problem. On the other hand, since there is almost a vertical jump in reduction of flow stress carrying capacity (see Figs. 8, 12, and 21 in Marchand and Duffy, 1988), it would be difficult to represent such drastic change of flow stress by a single constitutive relation that is responsible to describe both thermal–mechanical behaviors of matrix as well as the behaviors of the shear band in the post-bifurcation phase. The underling argument here is that separate constitutive description, or multiple physics model, is more convenient and efficient in constitutive modeling.

In the case of high strain rate loading, it has been speculated that there is an intensified high strain rate zone at the tip of a propagating shear band (e.g. Wright and Walter, 1987; Wright, 1995; Wright and Walter, 1996). Moreover, based on the observation of micrograph of shear band surfaces, there is uniform

void distribution throughout the shear band (Zhou et al., 1996b). It is thus suggested that dynamic shear band propagation may be related to damage evolution process, which is controlled by strain rate.

It is highly plausible that the magnitude of a strain rate in front of the shear band tip could be used as a criterion for the onset of stress collapse, or strain localization. It is possible that once the strain rate reaches a certain level, damage occurs within the shear band irreversibly, and the material changes its behavior inside the shear band, subsequently the material loses its stress carrying capability significantly, i.e. the stress collapse. On the other hand, by combining the notion of stress collapse with the notion of wave trapping (Wu and Freund, 1984), one may be able to explain the autonomous built-up of a high strain rate field in front of the shear band tip.

Zhou et al. (1996a, 1998) used a Newtonian flow constitutive relation to model the highly mobile plastic flow inside the shear band. Batra and Nechitailo (1997) used a compressible ideal fluid to model the shear band; recently, Raftenberg (2000) used a shear band softening model, which is based on experimental data (Raftenberg and Krause, 1999; Krause and Raftenberg, 1993), to simulate the post-bifurcation, or stress collapse state of the adiabatic shear band.

Stress collapse inside an adiabatic shear band is triggered by the attainment of a critical strain $\bar{\epsilon}_{\mathrm{cr}}$, which is controlled by strain rate. The stress collapses when the critical effective strain

$$\bar{\epsilon}_{\mathrm{cr}} = \epsilon_1 + (\epsilon_2 - \epsilon_1)\frac{\dot{\epsilon}_r}{(\dot{\epsilon}_r + \dot{\bar{\epsilon}})} \tag{56}$$

is reached, where ϵ_1, ϵ_2 and $\dot{\epsilon}_r$ are input parameters. After $\bar{\epsilon}$ reaches $\bar{\epsilon}_{\mathrm{cr}}$, the damaged material is assumed to behave like a non-Newtonian viscous fluid, so

$$\boldsymbol{\tau} = -\frac{\gamma[1 - J + \alpha(T - T_0)]}{J}\frac{E}{1 - v}\mathbf{1} + \mu_d(T)\mathbf{D} \tag{57}$$

where γ is the stiffness parameter and μ_d is the viscosity, which may be temperature dependent.

To simulate fracture and crack growth, a simple material damage algorithm is adopted in this work. The maximum tensile stress is used as the crack growth criterion. The algorithm works as follows: when the maximum tensile stress at a material point exceeds a certain limit, the crack is assumed to pass through that material point. To model the crack, the stress components are set to zero at that material point, and the value of temperature is set to room temperature.

The main advantages of using the critical stress based material damage algorithm is its simplicity. Because of the non-local nature of mesh-free approximation, the connectivity relation with respect to the referential configuration needs to be updated to prevent the particles on the other side of the crack from contributing over the crack line. A less accurate, but efficient way to get around a connectivity update is as follows: once a quadrature point within a background cell is damaged, then all the other quadrature points in the same background cell are considered to be damaged.

Since the specimen is 6 mm thick, the crack morphology observed in the experiment tend to be uniform in the thickness direction. Therefore, it may be reasonable to assume that the cleavage fracture toughness in the thermo-elasto-viscoplastic solid is controlled by the maximum circumferential stress, or hoop stress within the plane, which conforms with the conventional theory of brittle fracture (e.g. Erdogan and Sih, 1963). In our computation, the following criterion is used

$$\sigma_{\max} \geqslant \sigma_{\mathrm{cr}} \tag{58}$$

where the critical stress is set as $\sigma_{\mathrm{cr}} = 3\sigma_0$ (where σ_0 is the initial yield stress and $3\sigma_0$ is roughly the level of stress triaxiality expected at the tip of a crack in an elasto-plastic solid). When the maximum principal stress reaches $3\sigma_0$ at a material point (Gauss quadrature point), we set

$$\tau_{ij} = 0; \qquad T = T_0 \tag{59}$$

4. Numerical results

4.1. Overview

The computations carried out in this work focus on the experiments conducted by Rosakis and his co-workers, i.e. the ZRR problem. The experiment involves the asymmetric loading of a pre-notched plate (single notch) by a cylindrical projectile as shown in Fig. 3. In this numerical study, two configurations have been used to simulate plate specimens of different sizes, which correspond to two different sets of experiments. The first configuration models the experiment conducted by Zhou et al. (1996b) (see Fig. 4a), while the second one models the experiments conducted recently by Guduru et al. (2001) (see Fig. 4b). In the second experiment, there is a 2 mm long fatigue crack in front of the pre-notch, which increases the acuity of the crack. We have conducted both 2D and three-dimensional (3D) simulations for the first specimen: a 2D computation with projectile speed $V = 25$ m/s, and 3D computation with projectile speeds of $V = 33$ and 35 m/s respectively. A total 49,086 particles are used, with 32,080 background cells for the 3D numerical quadrature. There are eight quadrature points in each background cell, for a total of 256,640 Gauss quadrature points.

For the second specimen, we have only carried out a 2D computation with projectile speed $V = 37$ m/s. In all 2D computations the specimen is assumed to be in plane strain.

The primary objectives of this simulation are twofold: (1) to replicate failure mode transition; (2) to examine the growth criterion and driving force for dynamic shear band propagation.

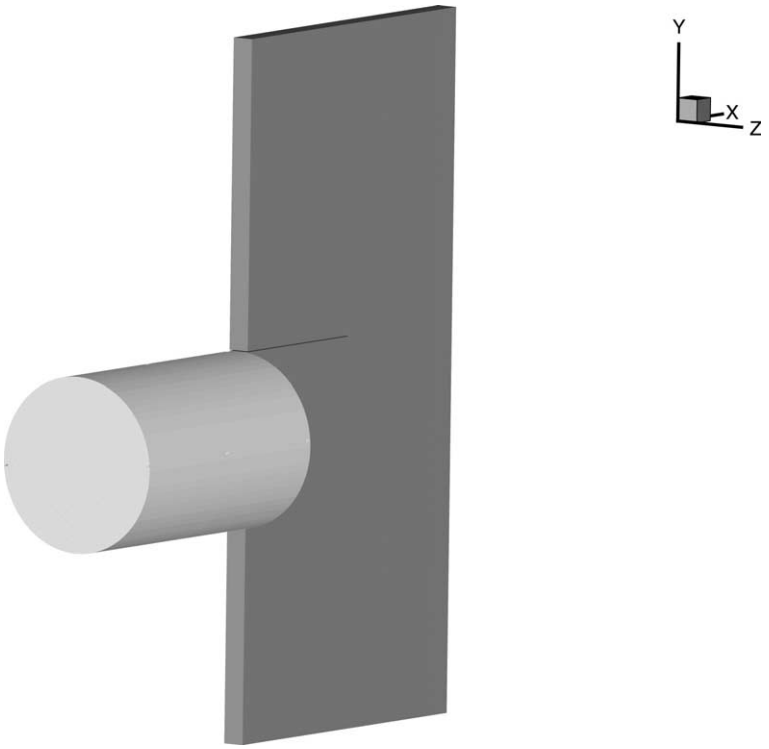

Fig. 3. The impact loaded plate with a re-notched crack.

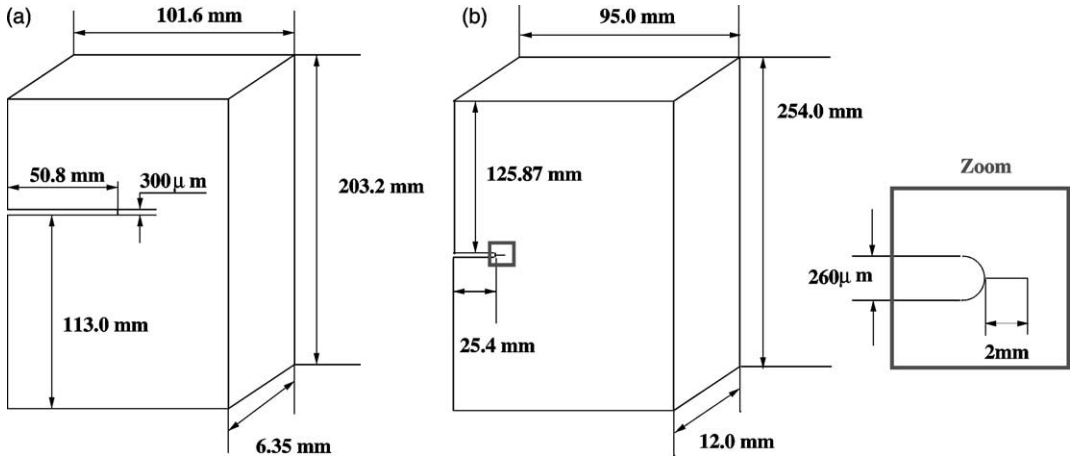

Fig. 4. The configuration of single notch specimens (a) specimen one, (b) specimen two.

4.2. Case I: intermediate speed impact ($V = 25$ m/s)

In the experiment conducted by (Zhou et al., 1996b), when the impact velocity is in the intermediate range, i.e. $20.0 < V < 30.0$ m/s, a shear band grows but is arrested within the specimen interior. The final failure of the specimen is caused by brittle fracture—a cleavage type crack forms and grows from the tip of the arrested shear band. This behavior differs from the original Kalthoff double notch experiment, where for impact velocities in the intermediate range, a crack directly initiates from the notch tip. The observation made by Zhou et al. (1996b) has far-reaching consequences. Few experiments, if any, have ever recorded such failure mode transition, i.e. the initial creation of a ductile failure mode (shear band) followed by a brittle failure mode under the same impact velocity; it sheds light on failure mode transition at high strain rates. It is, therefore, of considerable interest to simulate such a failure mode transition, to validate the numerical paradigm as well as to observe the detailed dynamic failure process "in slow motion". The main parameters in our simulation are listed in Table 1.

Fig. 5d–f shows the effective stress contours in the failure region following the impact. It can be clearly observed that a strip with lower effective stress initiates from the tip of the pre-notch, and grows steadily downwards.

At a certain point, it suddenly changes its direction, and grows upwards. This turning point is the point at which the shear band transforms into an opening crack. To clearly show the differences between the shear band and the resulting crack, we plot the same data by lowering the upper limit of the reference effective stress, and juxtapose the temperature contours in the failure area with the effective stress contours (Fig. 6). One may see that indeed there is a non-zero stress inside the downward part of strip, whereas in the upward part of the strip the effective stress is zero, which indicates the separation of the specimen. There is a quantitative agreement between the simulation (Fig. 5d–f) with the optical high speed camera observations (Fig. 5a–c).

In most experiments (e.g. Affouard et al., 1984; Giovanola, 1988a,b; Huang, 1987), it has been observed that cracks follow the path weakened by the growing shear band, whose origin has been attributed to either brittle fracture, or damage induced microvoid growth and coalescence. It is interesting that in our computations we observe a similar pattern of interface crack between the shear band and the matrix. Examining the details of Fig. 6, one may find that there is a zero stress region between the shear band and the rest of material in both effective stress contour and temperature profile, which indicates crack formation.

Table 1
Material parameters used in the computer simulations

Parameter	Value	Definition
$\dot{\epsilon}_0$	1×10^{-3} s^{-1}	Reference strain rate
m	70	Rate sensitivity parameter
σ_0	2000 MPa	Yield stress
ϵ_0	σ_0/E	Yield strain
n	0.01	Strain hardening exponent
T_0	293 K	Reference temperature
δ	0.8	Thermal softening parameter
κ	500 K	Thermal softening parameter
E	200 GPa	Young's modulus
v	0.3	Poisson's ratio
ρ	7830 kg m^{-3}	Mass density
c_p	448 J (kg K)$^{-1}$	Specific heat
α	11.2×10^{-6} K^{-1}	Coefficient of thermal expansion
χ	0.9	The fraction of plastic work converted to heat
ϵ_1	$4.0 \times \epsilon_0$	In Eq. (56)
ϵ_2	0.3	In Eq. (56)
$\dot{\epsilon}_r$	4.0×10^4 s^{-1}	In a range (1.0×10^4–6.0×10^4 s^{-1})
γ	0.002	
μ_d	5.0 Pa s	In a range (0.05–500.0 Pa s)
σ_{cr}	$3.0 \times \sigma_0$	Maximum tensile strength

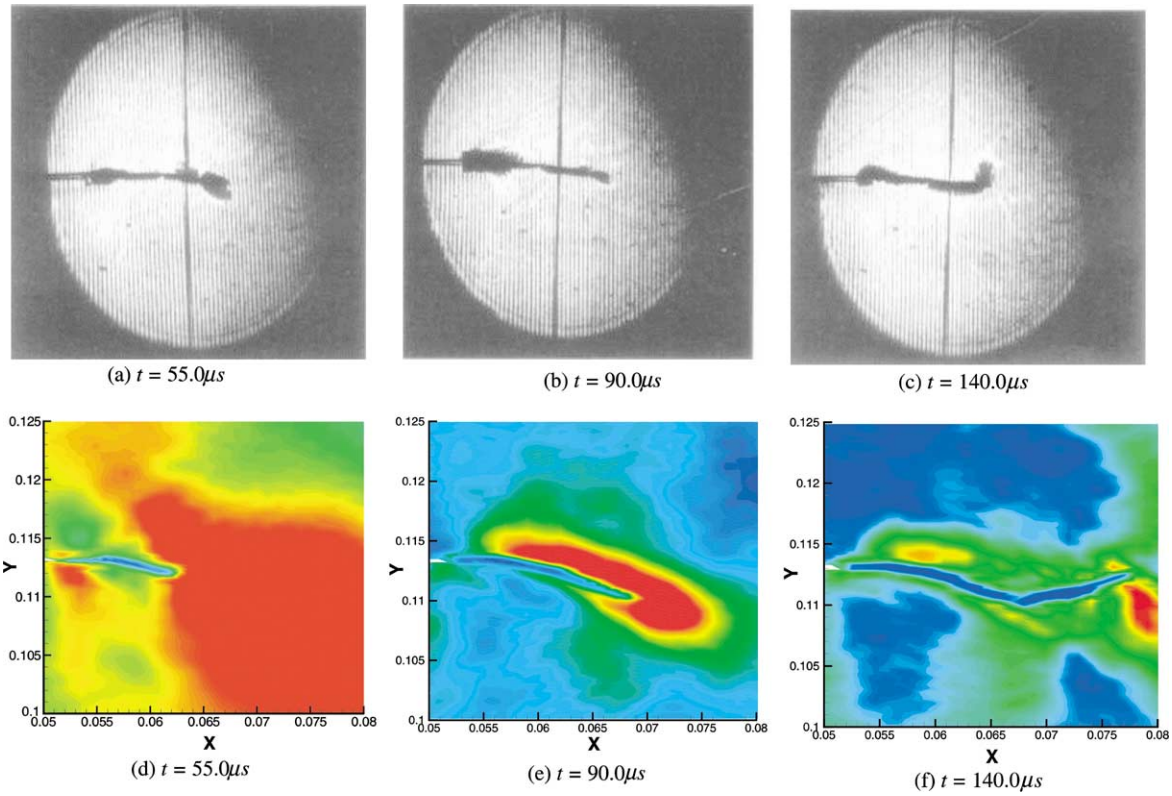

Fig. 5. Comparison between experimental results (a–c) (from Zhou et al., 1996b) and numerical results (d–f) (effective stress contour).

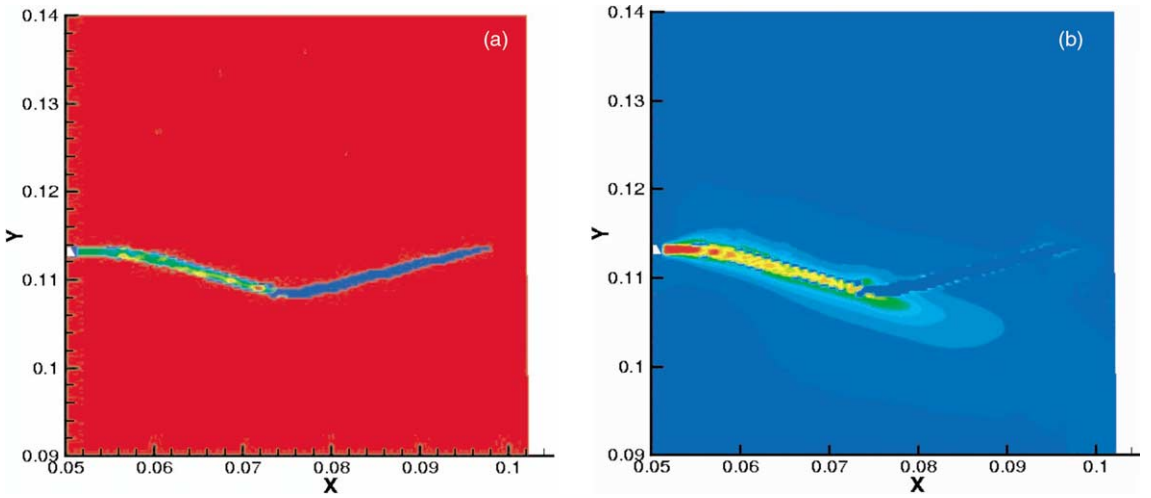

Fig. 6. The failure mode switching phenomenon (a) effective stress contour and (b) temperature contour.

4.3. Case II: high speed impact ($V = 33$ m/s)

When the impact velocity exceeds a certain limit [3] the cleavage fracture is suppressed, and a shear band initiates from the pre-notch tip and propagates through the specimen. Since the impact between the bullet and plate is asymmetric, the shear band propagates slightly downwards to form a curved path. Comparing with the intermediate impact speed range, one observes a failure mode transition, i.e. a transition from the cleavage type of fracture failure at lower impact speeds to ductile failure at higher impact speeds.

Mesh-free simulations accurately replicate this failure mode transition. A sequence of 3D results, which describe the evolution of the shear band, are displayed in Figs. 7 and 8 (effective stress contours) and Fig. 9 (temperature distributions). The stress states shown in Fig. 7 are the early states before the first elastic wave reaches the far end of the plate. The stress states shown in Fig. 8 are the states after shear elastic wave reaches the far end of the plate.

The experimental results (Zhou et al., 1996b) indicate that the shear band propagates along a curved surface. This shear band morphology is very difficult to capture by finite elements, because of the mesh alignment sensitivity that is inherent in such discretization. Using mesh-free methods, the curved shear band formation has been accurately captured in the computations presented here. To the authors knowledge, this is the first successful computation of the shear band propagation on a curved path.

In the 3D computations, a "temperature reflection" has been observed. That is, before the shear band reaches the end of the specimen, the temperature at the far side free surface has already risen (Fig. 10). A plausible explanation for this temperature reflection is that the plastic shear wave reaches the lateral free surface before the shear band, and the free-surface traction boundary condition amplifies the amplitude of the plastic wave, and causes the local temperature rise and the subsequent thermal softening at the free surface. It should be noted that this phenomenon has only been observed in the 3D simulations (see both Figs. 9 and 10). Fig. 10 gives a plane views of the temperature field as the shear band approaches the specimen edge.

[3] In the experiments conducted by Zhou et al. (1996a) this critical velocity is 29.6 m/s for C-300 steel. This value is expected to be sensitive to material as well as pre-notch geometry and specimen thickness.

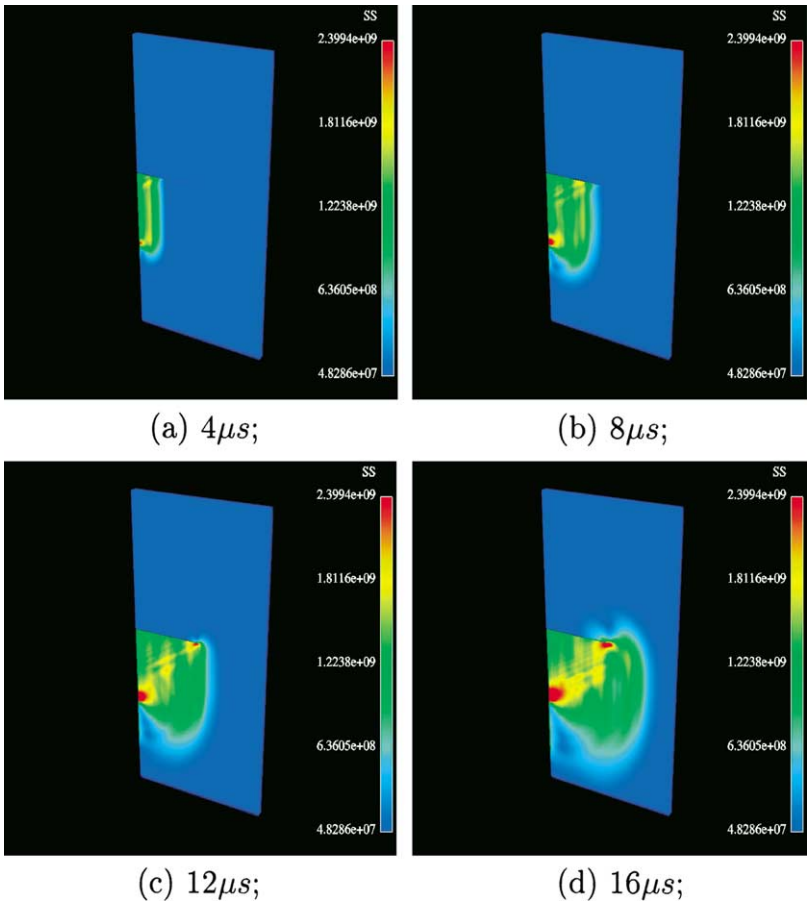

Fig. 7. 3D simulations: effective stress (SS) contours (Pa).

From Fig. 10, one may see that the computed shear band curves slightly down, but not as much as observed in the experiment. It is believed that this may be attributed to the acuity of the numerical crack. In the 3D computation, the crack tip of the pre-notch is modeled as a blunt cut, as shown in Fig. 11a. If one increases the acuity of the numerical pre-notch, by using the visibility condition (Belytschko et al., 1996) to model a zero-width fatigue crack (for implementation see Li et al., 2000).

Fig. 11b shows a 2D numerical fatigue crack configuration emanating from with the pre-notch. Using this model to increase the acuity of the pre-notch, we have predicted a curved numerical shear band (see Fig. 12b, with a curvature that agrees with that observed in the experiment by Zhou et al. (1996b) (see Fig. 12a). However, in the experiment, the shear band formed at an impact velocity $V = 29.6$ m/s, whereas in the computation, an impact velocity $V = 37$ m/s was used (Fig. 12b).

4.4. Some observations

In Fig. 13, the spatial strain rate (effective strain rate) distribution is juxtaposed with temperature signature of the adiabatic shear band. It shows that there is a strain rate concentration region right in the front the shear band tip. It indicates that there exists an asymptotic strain rate tensor field around the shear band

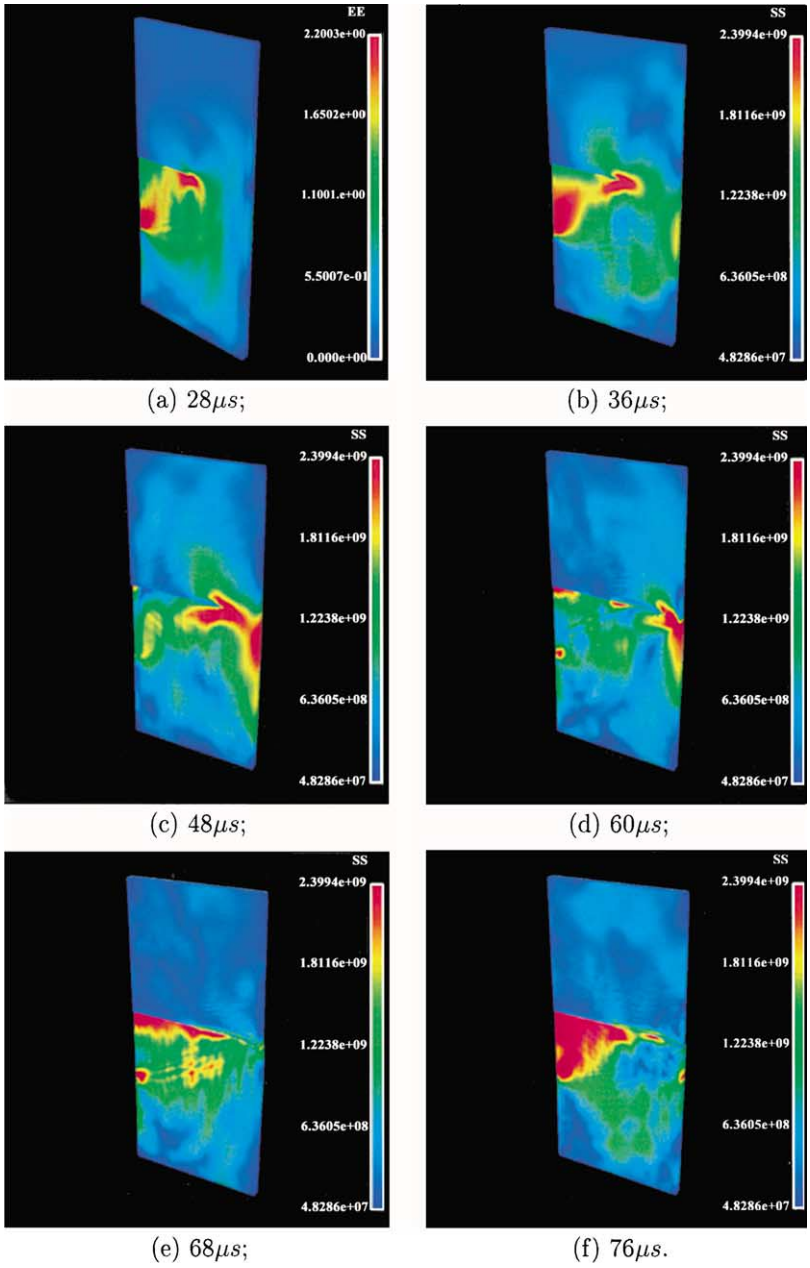

Fig. 8. 3D simulations: effective stress (SS) contours (Pa).

tip. We postulated that this high concentrated strain rate field is induced by the so-called "wave trapping" mechanism (see one-dimensional (1D) model by Wu and Freund (1984)). Based on Wu–Freund 1D linear (or logarithmic) rate sensitivity model, one may expect that the strain rate becomes unbound. To authors' knowledge, the simulations shown here is the first realization of wave trapping induced strain rate concentration in front of an adiabatic shear band tip in higher dimension. It is natural to compare asymptotic

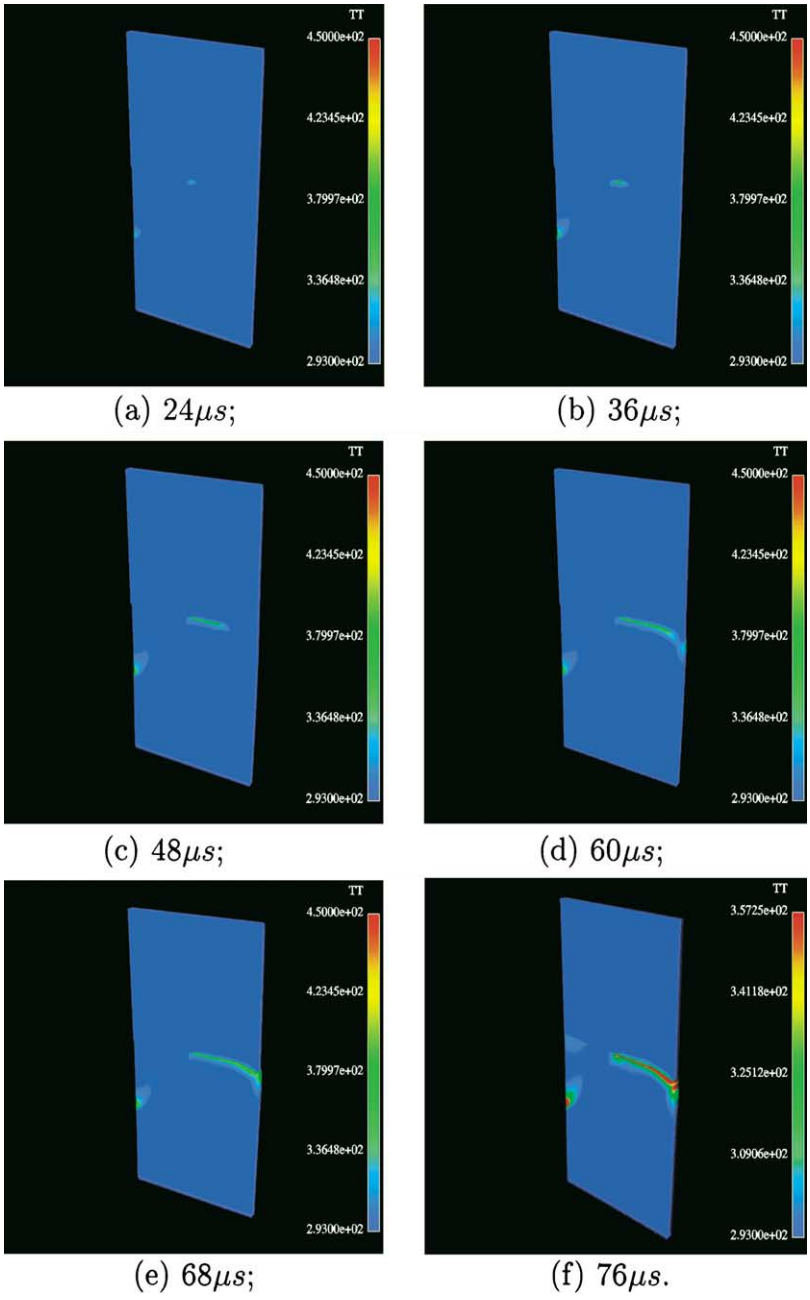

Fig. 9. 3D simulations: temperature (TT) contours (K°).

strain rate tensor field in front of a shear band with the asymptotic stress tensor field in front of a brittle crack.

Based on this analogy, it is speculated that adiabatic shear band propagation is controlled by the intensity of strain rate tensor field ahead of the shear band tip. After the strain rate reaches a certain level, it

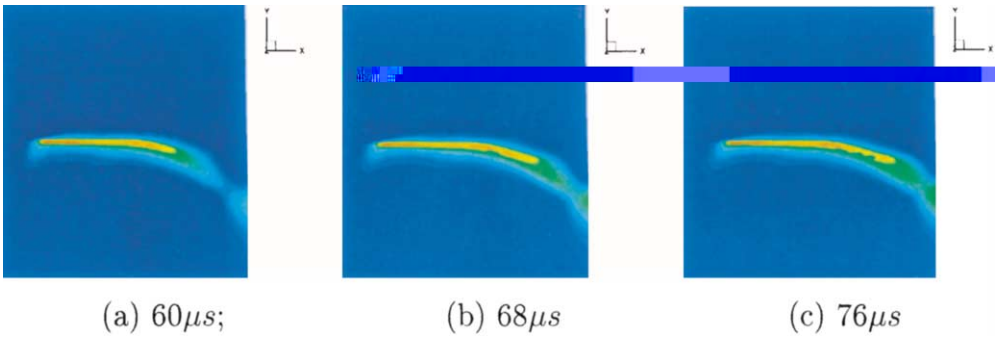

Fig. 10. Temperature reflection: 3D effect (a) 60 μs, (b) 68 μs and (c) 76 μs.

Fig. 11. Configuration of pre-notch and fatigue crack (a) pre-notch without fatigue crack (3D) and (b) pre-notch with fatigue crack (2D).

Fig. 12. Curved shear band formation: (a) experimental result and (b) numerical prediction ($V = 37$ m/s).